Journal of Inflammation Research

Dovepress
open access to scientific and medical research

Open Access Full Text Article

ORIGINAL RESEARCH

CD11b-Based Pre-Targeted SPECT/CT Imaging Allows for the Detection of Inflammation in Aortic Aneurysm

Xiaonan Zhou[1,2,*], Kai Zhu[1,2,*], Yiqiu Zhang[3–5,*], Yang Ming[1,2], Dai Shi[3–5], Hui Tan[3–5], Bitao Xiang[1,2], Shichao Zhu[1,2], Dengfeng Cheng[3–5], Hao Lai[1,2], Chunsheng Wang[1,2], Guobing Liu[3–5]

[1]Department of Cardiac Surgery, Zhongshan Hospital, Fudan University, Shanghai, 200032, People's Republic of China; [2]Shanghai Institute of Cardiovascular Diseases, Shanghai, 200032, People's Republic of China; [3]Department of Nuclear Medicine, Zhongshan Hospital, Fudan University, Shanghai, 200032, People's Republic of China; [4]Institute of Nuclear Medicine, Fudan University, Shanghai, 200032, People's Republic of China; [5]Shanghai Institute of Medical Imaging, Shanghai, 200032, People's Republic of China

*These authors contributed equally to this work

Correspondence: Guobing Liu, Department of Nuclear Medicine, Zhongshan Hospital, Fudan University, No. 180 in Fenglin Road, Shanghai, 200032, People's Republic of China, Tel +8618317086732, Fax +86-21-62489191, Email liu.guobing@zs-hospital.sh.cn; Chunsheng Wang, Department of Cardiac Surgery, Zhongshan Hospital, Fudan University, No. 180 in Fenglin Road, Shanghai, 200032, People's Republic of China, Email wangchunsheng@fudan.edu.cn

Purpose: To investigate the feasibility of a pre-targeted imaging strategy based on the cycloaddition between 1,2,4,5-terazine (Tz) and trans-cyclooctene (TCO) for evaluating CD11b expression in inflammatory aortic aneurysm (AA) using single photon emission computed tomography/computed tomography (SPECT/CT).

Methods: C57BL/6J mice were fed β-aminopropionitrile (1 g/kg/day) for 4 weeks to establish AA models. Anti-CD11b-TCO was synthesized and ^{99m}Tc-HYNIC-PEG$_{11}$-Tz was designed for pre-targeted SPECT/CT. The affinity and specificity of the probe for the inflammatory cell line Raw-264.7 were investigated. Then, anti-CD11b-TCO pre-targeted and ^{99m}Tc-HYNIC-PEG$_{11}$-Tz based SPECT/CT were performed to detect in vivo inflammation in AA. Finally, ex vivo aortic breast-specific gamma imaging (BSGI), Western blot assays, and immunohistochemical CD11b staining were performed to confirm the in vivo findings of SPECT/CT.

Results: In the AA models, 65.22% (15/23) had aortic lesions, including 43.48% (10/23) AA lesions. The anti-CD11b-TCO presented with a high TCO coupling ratio (7.43), and the ^{99m}Tc-HYNIC-PEG$_{11}$-Tz showed high radio-purity (>95%), good in vitro stability and a rapid clearance rate. Additionally, anti-CD11b-TCO and ^{99m}Tc-HYNIC-PEG$_{11}$-Tz presented high click rate (~89%). The in vitro clicked compound, ^{99m}Tc-HYNIC-PEG$_{11}$-Tz/TCO-anti-CD11b, showed high affinity and specificity for Raw-264.7 cells. ^{99m}Tc-HYNIC-PEG$_{11}$-Tz/TCO-anti-CD11b pre-targeting SPECT/CT successfully demonstrated inflammatory AA with a high AA-to-background ratio in AA mice, compared to AA mice that were injected with ^{99m}Tc-HYNIC-Tz/TCO-IgG (8.13 versus 3.71, $P < 0.001$) and control mice injected with ^{99m}Tc-HYNIC-Tz/TCO-anti-CD11b (8.13 versus 3.66, $P < 0.001$). This result was confirmed by ex vivo BSGI performed immediately after SPECT/CT and immunohistochemical CD11b staining.

Conclusion: SPECT/CT imaging using the anti-CD11b-TCO/Tz-PEG$_{11}$-HYNIC-^{99m}Tc based pre-targeting imaging strategy allows for the detection of inflammation in progressive AA.

Keywords: aortic aneurysm, inflammation, SPECT/CT, CD11b, macrophage

Introduction

Aortic aneurysm (AA) poses a heavy healthcare burden, as it is associated with a high mortality rate when it progresses into aortic dissection (AD) or rupture.[1,2] At present, surgical management is the main treatment method for AA, and the current guidelines recommend the cross-sectional diameter of the aorta as the criterion for making decisions about surgical intervention.[1] However, there are no significant clinical symptoms in the early or progressive stages of AA, and aortic diameter is not an ideal parameter for the early diagnosis of AA. Furthermore, it has been reported that fatal complications occurred in nearly 20–30% of patients with AA before the diameter criterion for surgery was met.[3]

Received: 30 November 2021
Accepted: 8 March 2022
Published: 16 March 2022

Therefore, fatal dissection complication or rupture may occur without obvious warning, inducing poor prognosis of the patients.[4] Accordingly, a method that can efficiently diagnose AA in its early stages is needed, but the current diagnostic techniques do not allow for the early diagnosis of AA.[5]

Inflammation is considered to be the main factor involved in the formation and progression of AA.[6] In the early stage, inflammatory cells, mainly macrophages, extensively infiltrate the aortic wall.[7,8] Cytokines, matrix-degrading proteases, and reactive oxygen species are highly associated with infiltration of inflammatory cells, and implicated in the formation of AA. Further, matrix metalloproteinases (MMPs), which play a central role in vascular remodeling as one of the endopeptidases, are mainly secreted by inflammatory cells.[9,10] Therefore, inflammatory cells could be a potential target for the evaluation of AA in its early stage.

Integrin αM (CD11b), which is encoded by the integrin subunit alpha M (ITGAM) gene, has been recognized as the surface marker of monocytes or macrophages.[11] Previously, CD11b targeting and imaging with ^{99m}Tc-labelled anti-CD11b probe and SPECT/CT has been applied in the evaluation of atherosclerosis.[12] Given the close association between inflammation and AA, this imaging strategy could also be applied for the diagnosis and evaluation of AA.

However, despite the excellent target affinity and specificity of monoclonal antibody (mAb)-based imaging, the use of monoclonal antibodies is limited by their high molecular weight, poor tissue infiltration, and slow pharmacokinetics, which might expose healthy organs to high levels of radiation. Given these limitations, a pre-targeting imaging strategy could be advantageous. In this strategy, a modified mAb is administered with a fixed duration to ensure accumulation at the target site. Then, a small-molecular-weight radioligand that can conjugate with the pre-targeted mAb can be injected for imaging (any unbound radioligand is cleared quickly on account of its small molecular weight).[13,14] The most promising pre-targeting methodology is based on inverse electron demand [4 + 2] Diels-Alder (IEDDA) cycloaddition between 1,2,4,5-terazine (Tz) and trans-cyclooctene (TCO), which has been widely used in tumor imaging but rarely used in the imaging of cardiovascular diseases over the last few decades.[14–18] Such a method may have potential for the diagnosis of AA in its early stage through the detection of an inflammatory marker. Therefore, the aim of the current study was to investigate the feasibility of the IEDDA pre-targeting method in evaluating CD11b expression in a mouse model of inflammation-associated AA.

Materials and Methods

Ethical Approval

This study was approved by the ethics committee of Zhongshan Hospital, Fudan University, and all the experiments were performed in accordance with the guidelines and regulations of this committee.

Establishment of Animal Model

Three-week-old male C57BL/6J mice were obtained from Shanghai SLAC Laboratory Animal Co. Ltd. (Shanghai, China) and maintained on a normal diet. The experimental group was administered β-aminopropionitrile (BAPN) (A13043, Alfa Aesar, USA) dissolved in drinking water (1 g/kg) every day for 4 weeks. The control group was provided a regular diet and clean water and kept under the same conditions.

Conjugation of the Anti-CD11b Antibody with the TCO-NHS Ester

Anti-CD11b-Ab (130 kDa) targeting the α [M] chain of Mac-1 (CD11b/CD18, α [M]β 2 integrin) was purchased from BD Biosciences (New Jersey, USA) and was conjugated to the amine-reactive TCO-NHS ester (Click Chemistry Tools, Scottsdale, Arizona, USA) following the procedure described in Section 1of the supplementary file. The concentration of the product was determined based on its absorbance at 280 nm using EC280 (~2.267 $[mg/mL]^{-1}cm^{-1}$). The purity and aggregation of the product were determined with size-exclusion chromatography column-high performance liquid chromatography (SEC-HPLC). The drug-to-antibody ratio (DAR) of the product was determined by liquid chromatography-mass spectrometry (LC-MS) according to the following equation.

$$\mathrm{DAR} = \frac{\sum_i Area_i \times DAR_i}{\sum_i Area_i}$$

Synthesis of HYNIC-PEG$_{11}$-Tz and Radiolabeling with ^{99m}Tc

HYNIC-PEG$_{11}$-Tz was synthesized from three commercially available compounds: 3-(4-benzylamino)-1,2,4,5-tetrazine (Tz) bearing an amine-reactive linker, O-(2-aminoethyl)-O′-[2-(boc-amino)ethyl]-decaethylene glycol (NH2-PEG$_{11}$-NHBoc), and 6-hydrazinonicotinyl (HYNIC) bearing Boc protection. The detailed procedures are presented in Section 2 of the supplementary file. The radiolabeling of HYNIC-PEG$_{11}$-Tz with ^{99m}Tc using tricine as a co-ligand is summarized in Figure 1A. Briefly, HYNIC-PEG$_{11}$-Tz was dissolved in water at a concentration of 1 mg/mL and stored at −20°C. For radiolabeling, 20 μg of the HYNIC-PEG$_{11}$-Tz solution was brought to room temperature and added to 200 μL tricine solution (concentration: 100 mg/mL in water). Then, 1 μL of freshly prepared $SnCl_2$ solution (1 mg/mL in 10^{-3} M HCl) and 185 MBq of $Na^{9m}TcO_4$ (< 100 μL) were added. The pH of the mixture was adjusted to 5.0 with HCl. After gentle vortexing, the combined solution was incubated for 20 min. Labeling efficiency was tested using HPLC (Agilent, Shanghai, China) equipped with a Gemini 5-μm NX-C18 reversed-phase column, and water/0.1% TFA (A) and ACN/0.1% TFA (B) were used as the mobile phases (15% to 45% B in 20 min). The in vitro stability in NaCl (0.9%), PBS (0.01 M), and BSA solutions was evaluated for up to 8 h at 25°C using radio-HPLC. The fraction of intact ^{99m}Tc-HYNIC-PEG$_{11}$-Tz was calculated by integrating the peak corresponding to the compound and dividing it by the integral for the whole HPLC run.

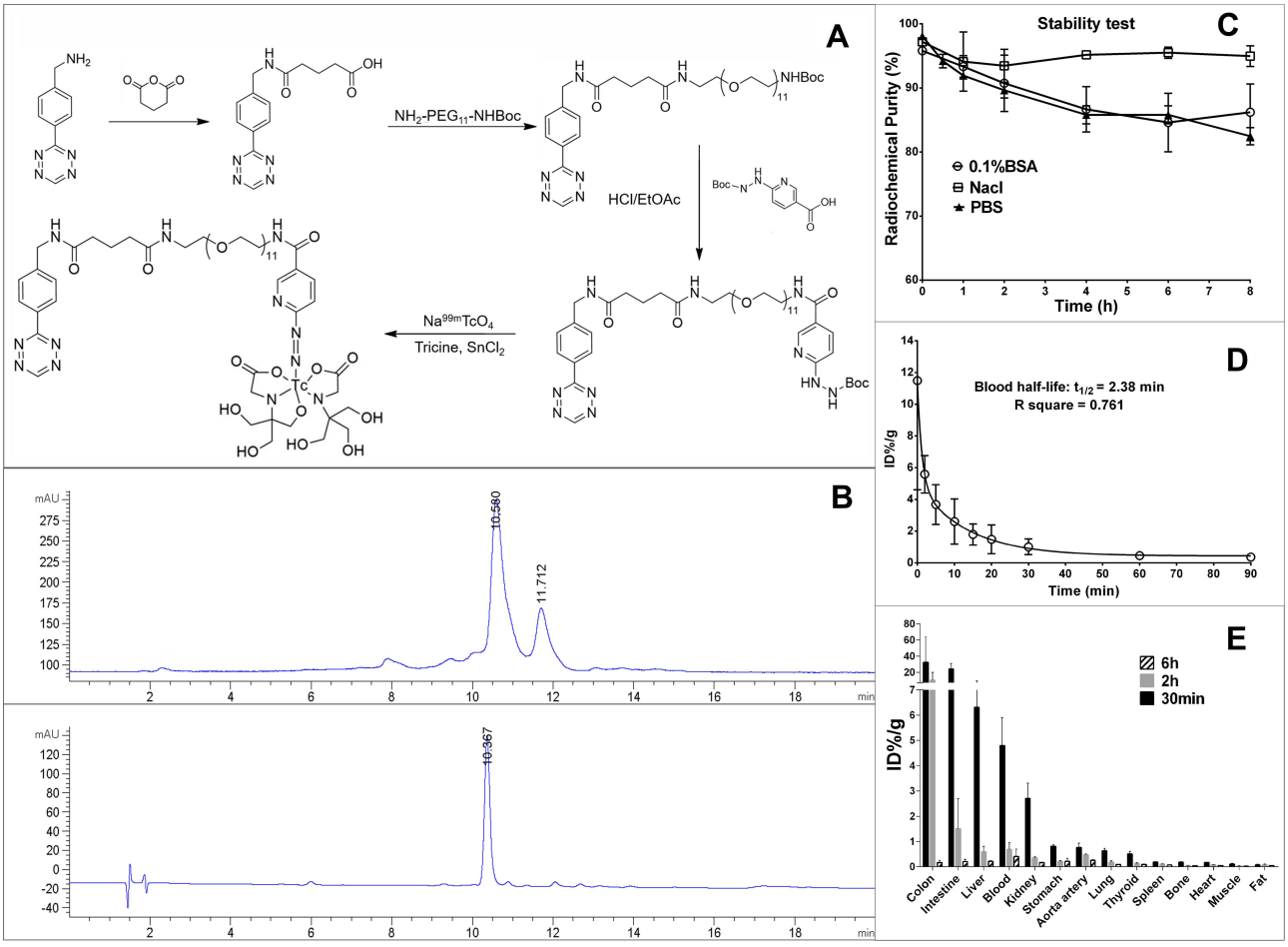

Figure 1 Synthesis and characterization of ^{99m}Tc-HYNIC-PEG$_{11}$-Tz. (**A**) Schematic diagram depicting the main steps of ^{99m}Tc-HYNIC-PEG$_{11}$-Tz synthesis. (**B**) RP-HPLC analysis of ^{99m}Tc-HYNIC-PEG$_{11}$-Tz showing its radio profile (Retention time [Rt] = 10.58 min, top) and ultra-violet profile (Rt = 10.2 min, wavelength = 280 nm, bottom). The radiolabeled isomer was identified in the RP-HPLC curve (Rt = 11.71 min, top). (**C**) In vitro stability of ^{99m}Tc-HYNIC-PEG$_{11}$-Tz in BSA, NaCl and PBS solutions for 8 h after labelling. (**D**) Half-life of ^{99m}Tc-HYNIC-PEG$_{11}$-Tz in blood. (**E**), Biodistribution of ^{99m}Tc-HYNIC-PEG$_{11}$-Tz in C57BL/6J mice at 30 min, 2 h and 6 h after administration.

Pharmacokinetics and Biodistribution of ^{99m}Tc-HYNIC-PEG$_{11}$-Tz

^{99m}Tc-HYNIC-PEG$_{11}$-Tz (1.6 μg/400 μCi per mouse) was injected into five C57 mice (male, 8 weeks old) via the tail vein to evaluate blood pharmacokinetics, and it was injected into 15 C57 mice (male, 8 weeks old) to investigate in vivo biodistribution. The half-life of ^{99m}Tc-HYNIC-PEG$_{11}$-Tz in blood was determined through serial blood collection from the tail vein after injection. For the biodistribution study, five mice per group were killed at 30 min, 2 h and 6 h after administration of ^{99m}Tc-HYNIC-PEG$_{11}$-Tz and their organs were harvested. Each sample was weighed and assessed with a γ counter (CRC-15R; Capintec Inc., Ramsey, NJ). After the data were corrected for radioactive decay, the percentage of ^{99m}Tc-HYNIC-PEG$_{11}$-Tz per injected dose per gram tissue (ID%/g) was calculated. The mean blood half-life of ^{99m}Tc-HYNIC-PEG$_{11}$-Tz was then estimated by mono-exponential decay via GraphPad Prism 6.01 (GraphPad Software Inc.).

In vitro Ligation of ^{99m}Tc-HYNIC-PEG$_{11}$-Tz with Anti-CD11b-TCO

The reaction between ^{99m}Tc-HYNIC-PEG$_{11}$-Tz and anti-CD11b-TCO was tested in PBS (n = 3). First, 100 μg anti-CD11b-TCO was incubated with ^{99m}Tc-HYNIC-PEG$_{11}$-Tz at a molar ratio of 1:1 at 37°C for 30 min. Then, 20 μL of the combined solution was uploaded to an SEC-HPLC (1260 Infinity, Agilent Technologies) with PBS as the mobile phase at a flow rate of 0.7 mL/min. The fraction of ligated compound was calculated as the ratio of the integrated corresponding radioactive peak divided by the integral for the whole HPLC run.

Cell Binding Assay

Raw-264.7 cells and human umbilical vein endothelial cells (HUVECs) were purchased from Shanghai Zhong Qiao Xin Zhou Biotechnology Co. Ltd. (Shanghai, China). The Raw-264.7 cells were used to test the cellular affinity of the ligated ^{99m}Tc-HYNIC-Tz/TCO-anti-CD11b, with HUVEC cells as the negative control. The Raw-264.7 cells were cultivated in a 24-well plate (1×10^6 cells/well) overnight. Then, all the wells were rinsed with PBS, and a concentration gradient of the ligated compound (3–123 nM) was added to the wells as a probe and incubated at 37°C for 2 h. The total volume of each well was 0.5 mL. For nonspecific binding, the same amount of probe was added to each well, which did not contain cells but an equal volume of Dulbecco modified Eagle medium. For evaluating cell binding, the cells were rinsed twice with PBS and the supernatant was removed. Then, the cells remaining in each well were collected for γ counting. The same process was followed for Raw-264.7 cells incubated with ^{99m}Tc-HYNIC-Tz/TCO-IgG and HUVEC cells incubated with ^{99m}Tc-HYNIC-Tz/TCO-anti-CD11b. For the blocking experiments, Raw-264.7 cells were incubated with 50-fold excess unlabeled anti-CD11b antibody 2 h prior to incubation with ^{99m}Tc-HYNIC-Tz/TCO-anti-CD11b. All the experiments were conducted in triplicate. After each cellular experiment, the 24-well plates were imaged with BSGI for overall visualization of cellular affinity.

Pre-Targeted SPECT/CT Imaging and Analysis

Before imaging, anti-CD11b-TCO (~100μg/mouse) was intravenously administered to five AA mice and five control mice via the tail vein, while IgG-TCO of the same dose was injected in five other AA mice. After an accumulation interval of 24 h for pre-targeting, the same mice were injected with ^{99m}Tc-HYNIC-PEG$_{11}$-Tz (~1 mCi/mouse), also via the tail vein. Two hours later, micro-SPECT/CT scanning was conducted on all the mice with the Nano SPECT/CT scanner (Bioscan, Washington DC, USA) equipped with four high-resolution conical collimators and 9-pinhole plates. CT was performed first with the following parameters: tube voltage, 45 kVp; current, 0.15 mA; resolution matrix, 256 × 512; exposure time, 500 ms/frame; total time, 7 min. Then, SPECT was performed with the mice in the same position, using the following parameters: energy peak, 140 keV; window width, 10%; matrix, 256 × 256; resolution, 1 mm/pixel; scan time, 35s/projection with 24 projections in all. The SPECT images were reconstructed using three-dimensional ordered-subset expectation maximization with the HiSPECT algorithm.

SPECT/CT data were transferred to the InVivoScope software (Version 1.43; Bioscan, Washington DC, USA) for post processing. Identical regions of interest (ROIs) were drawn in the aneurysm area and in area of surrounding muscle (as the background) to determine the concentration of radioactivity (mCi/mm^3). Then, a normalized signal ratio of the aneurysm to the background (A/B ratio) was calculated for inter-mice comparison.

Ex vivo Planar Imaging of Whole Aorta Specimens

Immediately after SPECT/CT imaging, the whole aorta of the mice were dissected and imaged with breast-specific gamma imaging (Dilon 6800; Dilon Technologies, Newport News, VA) for ex vivo planar imaging, which provided a more direct visualization of radioactivity distribution in the whole aorta. The imaging parameters were as follows: high-resolution collimator; peak energy, 140 keV; window width, 10%; matrix, 80 × 80; resolution, 0.32 mm/pixel. The collection time was 15−20 min, with total counts of 80,000 to 100,000.

Histological Evaluation

All aortic specimens from the mice that underwent in-vivo SPECT/CT imaging were selected for histological evaluation. The aorta of the control group mice was used as the blank control, and the experimental group was divided into the AA and Aortic dissecting aneurysm groups according to the anatomical observations. Briefly, the resulted aortas were fixed in formalin, dehydrated, embedded in paraffin and then sliced at the lesion area. Serial sections (with a thickness of 5 μm) were prepared for hematoxylin-eosin (HE) staining and CD11b staining. An Olympus BX35 microscope equipped with a Nikon DS-Fil camera (Japan) was used for microscopy and imaging.

Western Blot Analysis

Aortic specimens from the experimental group and control group mice were stored in liquid nitrogen for Western blot assays to evaluate the expression of CD11b and MMP. Protein from the aortic specimens was extracted with radio immunoprecipitation assay (P0013B, Beyotime) and phenylmethylsulfonyl fluoride (ST506, Beyotime), and then measured with the bicinchoninic acid assay kit (P0012S, Beyotime). The lysates containing 40 μg protein were treated by SDS-PAGE and separated by electrophoresis. The isolated proteins were transferred to a polyvinylidene fluoride (PVDF) membrane. Then, the PVDF membrane was blocked in tris buffered saline with Tween (TBST) containing 5% skim milk, and a primary antibody solution was prepared with TBST containing 3% BSA. The membrane was incubated overnight at 4°C with one of the following primary antibodies each time: anti-CD11b (EPR1344, Abcam), anti-MMP-9 (ab236494, Abcam), and anti-β-actin (ab8227, Abcam) antibodies. Then, it was washed three times with TBST, incubated at room temperature for 1 h with secondary antibody (diluted 1:5000), washed three times with TBST again, and exposed.

Statistical Analysis

We used GraphPad Prism 6.0 (GraphPad Software Inc.) for statistical analysis. Data are presented as mean ± standard deviation. Differences between groups were tested using the Student's *t*-test or one-way ANOVA with Tukey's method for post-hoc comparisons. All hypothesis tests were two sided, and the significance levels were set as $P < 0.05$.

Results

Probe Synthesis and Characterization

Detailed information regarding the synthesis and characterization of anti-CD11b-TCO is provided in Section 1 of the supplementary file. The purity of the product was 93.14%, with an aggregation level of 6.86%, as determined with SEC-HPLC. LC-MS confirmed the presence of an average of 7.43 TCO moieties per anti-CD11b-Ab molecule. Detailed procedures for the synthesis and characterization of HYNIC-PEG_{11}-Tz are provided in Section 2 of the supplementary file. After purification with prep-HPLC and characterization with LC-MS, the final product, HYNIC-PEG_{11}-Tz, had a high purity (90.0%) and was in the form of a red solid substance. For labelling with ^{99m}Tc, HYNIC-PEG_{11}-Tz was incubated with $Na^{99m}TcO_4$ at room temperature for 15 min in the presence of $SnCl_2$ as a reductant and tricine as a co-ligand (pH = 5.0, Figure 1A). The radiolabeled ^{99m}Tc-HYNIC-PEG_{11}-Tz had high specific activity of 9.25 MBq/μg and high radiochemical purity of more than 95%, as confirmed by reversed-phase HPLC (RP-HPLC), and thus, further purification was not necessary. Radiolabeled isomers were identified by RP-HPLC (Figure 1B), which might indicate molecules radiolabeled on the HYNIC moiety.[19] The in vitro cycloaddition reaction between ^{99m}Tc-HYNIC-PEG_{11}-Tz and anti-CD11b-TCO occurred rapidly under aqueous conditions without the addition of catalysts and resulted in nearly complete conversion, with the 1:1 Tz-to-Ab reaction providing a yield of 89.35% ± 3.16%, as shown in Figure 1B.

Stability, Kinetics, and Biodistribution of ^{99m}Tc-HYNIC-PEG$_{11}$-Tz

The radiolabeled ^{99m}Tc-HYNIC-PEG$_{11}$-Tz demonstrated favorable stability in NaCl, PBS, and BSA solutions for at least 8 h after labelling (Figure 1C). With regards to the in vivo kinetics of ^{99m}Tc-HYNIC-PEG$_{11}$-Tz, it had a half-life of 2.38 ± 0.93 min (Figure 1D) in blood; this indicates quick clearance from blood. The biodistribution of ^{99m}Tc-HYNIC-PEG$_{11}$-Tz in C57 mice at 30 min, 2 h and 6 h after injection is shown in Figure 1E. ^{99m}Tc-HYNIC-PEG$_{11}$-Tz was characterized by rapid tissue distribution and subsequent clearance mainly from the hepatobiliary system to intestine-colon system due to its appropriate lipophilicity. Quick clearance of the radiotracer from the kidney was also observed (from 2.71% ± 1.03%ID/g at 30 min to 0.17% ± 0.038%ID/g at 6 h); this finding indicates that ^{99m}Tc-HYNIC-PEG$_{11}$-Tz has both renal and hepatobiliary elimination pathways. It is noteworthy that uptake of ^{99m}Tc-HYNIC-PEG$_{11}$-Tz in the thyroid and stomach was low (<1% ID/g), which illustrates that the radiotracer has high in vivo stability.

Affinity and Specificity of the Engineered Probe for Inflammatory Cells

The in vitro ligation between ^{99m}Tc-HYNIC-PEG$_{11}$-Tz and anti-CD11b-TCO reached a high conversion rate of 89% (Figure 2). The ligated compound showed high affinity for the inflammatory Raw-264.7 cells, with a K_D value of 1.93 ± 0.30 nM and a B_{max} value of 3.78 ± 0.15×10^5 receptors/cell (Figure 3A). The un-ligated ^{99m}Tc-HYNIC-PEG$_{11}$-Tz and the isotype-IgG ligated ^{99m}Tc-HYNIC-PEG$_{11}$-Tz/TCO-IgG had significantly lower affinity for Raw-264.7 cells than ^{99m}Tc-HYNIC-PEG$_{11}$-Tz/TCO-anti-CD11b (Figure 3B). In addition, ^{99m}Tc-HYNIC-PEG$_{11}$-Tz/TCO-anti-CD11b exhibited almost no affinity for HUVEC cells (Figure 3B). To further confirm the specific affinity of the ligated probe for the Raw-264.7 cell line, we performed blocking studies with 50-fold un-modified anti-CD11b-Ab at the same concentration gradient as ^{99m}Tc-HYNIC-PEG$_{11}$-Tz/TCO-anti-CD11b. The findings showed obvious blocking of CD11b on the membrane of Raw-264.7 cells (Figure 3B), with statistically significant differences between the unblocked and blocked groups at all concentration points. BSGI imaging of the 24-well plate performed immediately after each cell binding assay provided an overall visualization of the affinity and specificity of the probe, as shown in Figure 3C–E, and the CT image of the 24-well plate is shown in Figure 3F.

Animal Models of AA

There was no AA formation and no mouse died in the control group (0/8) (Figure 4A–C). In the experimental group, four mice died from AA rupture before the end of the experiment. The mortality rate of the experimental group was 17.39% (4/23), which was not significantly different from that of the control group ($P > 0.05$) (Figure 4B). In the experimental

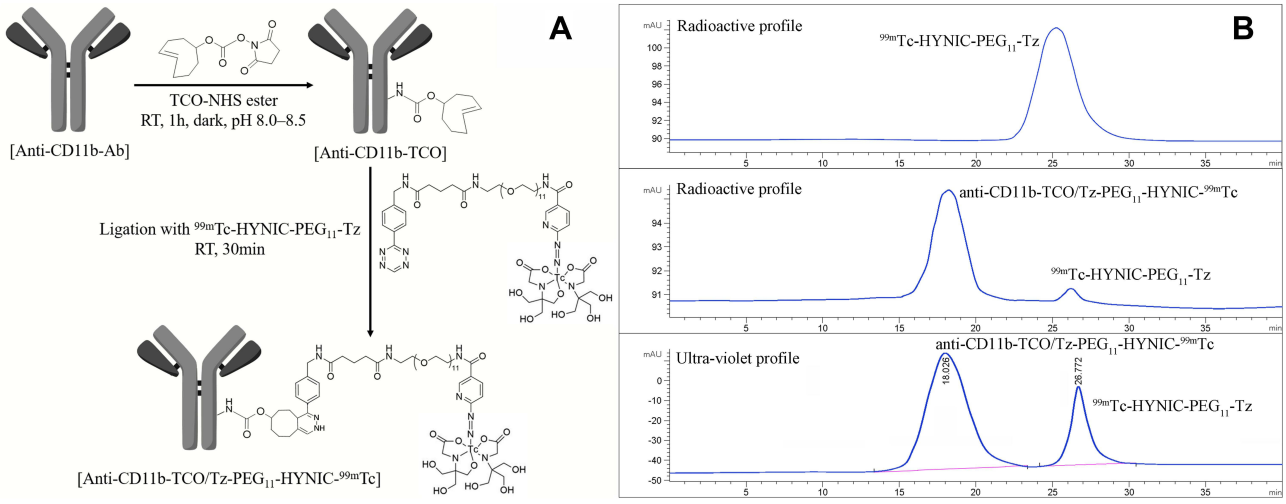

Figure 2 Synthesis and characterization of anti-CD11b-TCO/Tz-PEG$_{11}$-HYNIC-^{99m}Tc. (**A**) Schematic diagram illustrating the synthesis of anti-CD11b-TCO/Tz-PEG$_{11}$-HYNIC-^{99m}Tc. (**B**) SEC-HPLC presenting the reaction between anti-CD11b-TCO and ^{99m}Tc-HYNIC-PEG$_{11}$-Tz. Top, radioactive profile of ^{99m}Tc-HYNIC-PEG$_{11}$-Tz (Rt = 26.77 min); middle, radioactive profile of anti-CD11b-TCO/Tz-PEG$_{11}$-HYNIC-^{99m}Tc (Rt = 18.03 min); bottom, the 280-nm ultra-violet profile of the anti-CD11b-TCO/Tz-PEG$_{11}$-HYNIC-^{99m}Tc complex. The conversion rate was 89%.

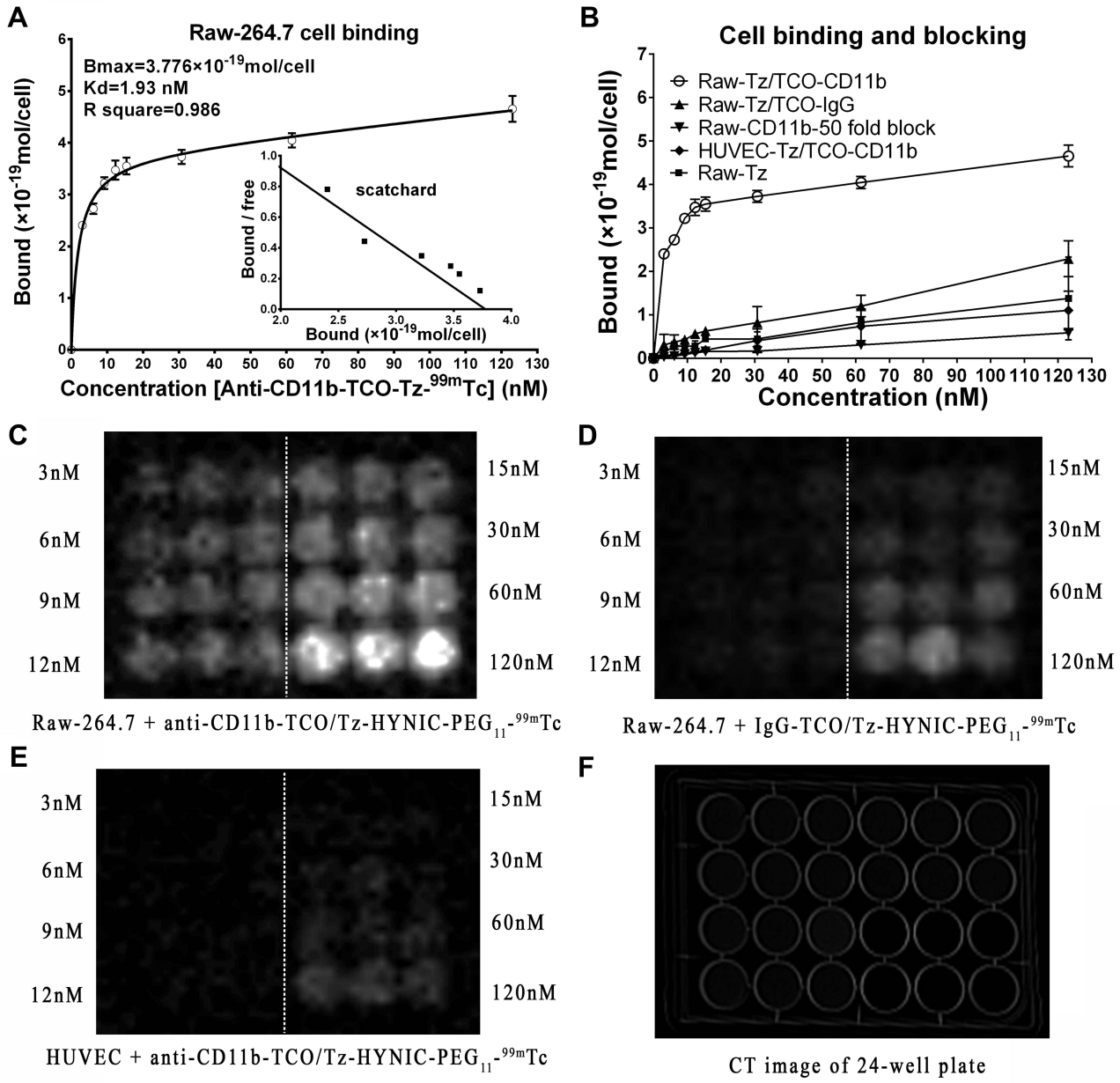

Figure 3 In vitro cellular binding and blocking assays. (**A**) Saturation binding curve generated by incubating the Raw-264.7 cells with ligated ^{99m}Tc-HYNIC-PEG$_{11}$-Tz/TCO-anti-CD11b. The inset shows the corresponding Scatchard plot. (**B**) Saturation binding and blocking curves indicating the specificity and affinity of Raw-264.7 cells for ligated ^{99m}Tc-HYNIC-PEG$_{11}$-Tz/TCO-anti-CD11b. (**C** and **D**) are planar gamma images of the 24-well plate with Raw-264.7 cells incubated with ligated ^{99m}Tc-HYNIC-PEG$_{11}$-Tz/TCO-anti-CD11b and ^{99m}Tc-HYNIC-PEG$_{11}$-Tz/TCO-IgG, respectively. (**E**) Planar gamma image of the 24-well plate with HUVEC cells incubated with ligated ^{99m}Tc-HYNIC-PEG$_{11}$-Tz/TCO-anti-CD11b. (**F**) CT imaging of the 24-well plate. The white dashed lines in (**C**–**E**) indicate that the experiments were performed in triplicate with each of the concentrations shown on both sides.

group, 65.22% (15/23) of the mice had aortic lesions, including AA in 43.48% (10/23) of the mice, and 60.87% (14/23) of the mice had aortic dilation (Figure 4C). Aortic diameter was measured in all the mice except for the four dead mice. The mean diameters of the ascending aorta (1.763 mm vs 1.13 mm, $P < 0.01$) and aortic arch (1.951 mm vs 1.328 mm, $P < 0.001$) of the mice from the experimental group were significantly higher than those of the mice in the control group. The mean diameter of the descending aorta (mean, 1.22 mm) was not significantly different between the two groups (1.22 mm vs 1.02 mm, $P > 0.05$; Figure 4D).

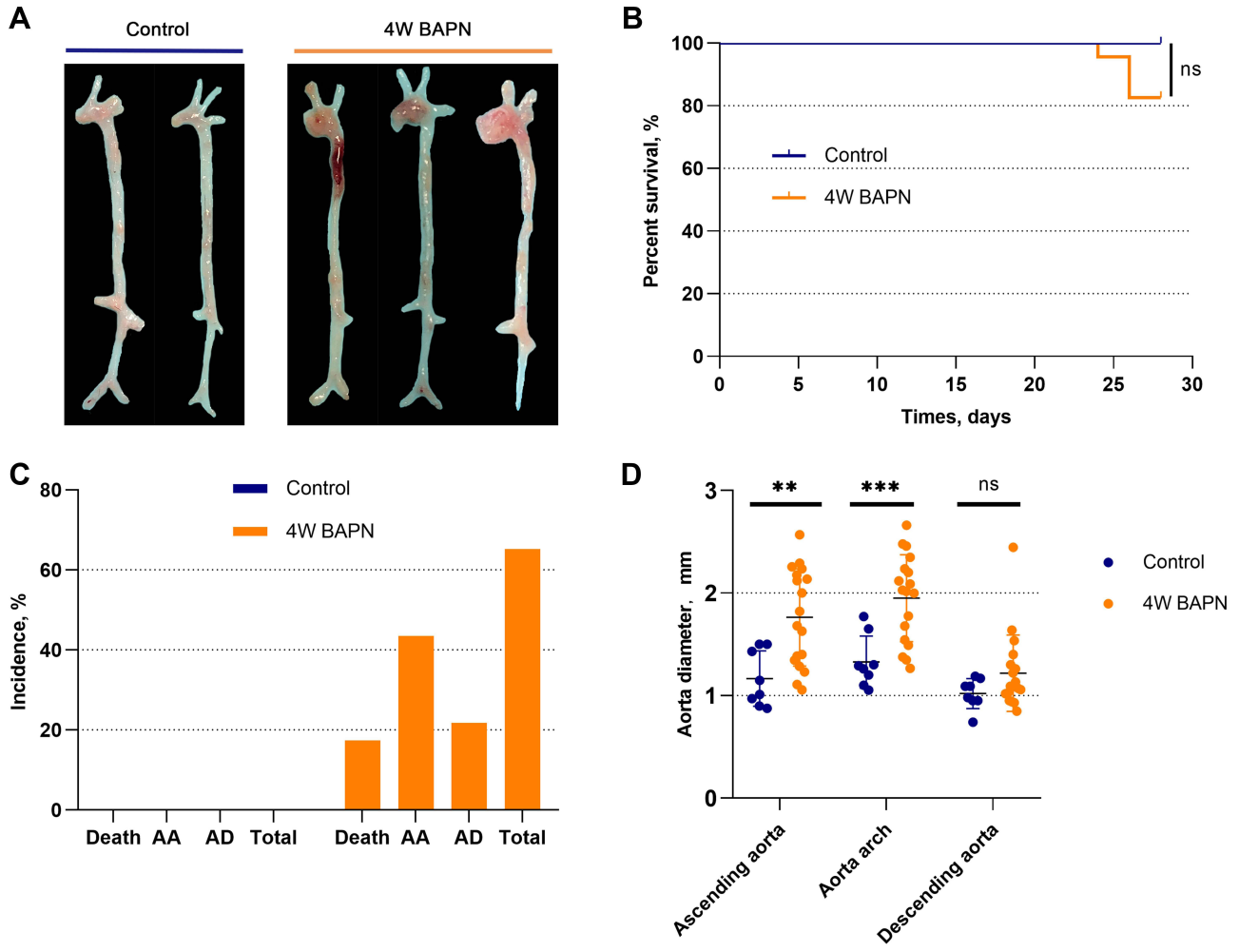

Figure 4 Establishment of AA mouse models. (**A**) Aortas of the control group and experimental group. (**B**) Comparison of survival curve between groups. (**C**) Statistical summary of aortic dissection/aortic aneurysm formation. (**D**) Comparison of the aortic diameter of different sites between groups. ** and *** indicate statistical significance at *P* values of <0.01 and <0.001, respectively.
Abbreviation: NS, the difference is not significant.

In-vivo SPECT/CT Imaging of Inflammation in AA

In anti-CD11b-TCO pre-targeted ^{99m}Tc-HYNIC-PEG$_{11}$-Tz micro-SPECT/CT imaging, the AA mice presented with significantly higher radioactivity in the AA areas compared with the corresponding areas of mice from the control group (A/B ratio: 8.13 ± 2.51 vs 3.66 ± 1.01, $P < 0.001$; Figure 5A, C, and D). In addition, in the AA group, anti-CD11b-TCO pre-targeted ^{99m}Tc-HYNIC-PEG$_{11}$-Tz micro-SPECT/CT imaging demonstrated higher radioactivity in the AA areas than IgG-TCO pre-targeted ^{99m}Tc-HYNIC-PEG$_{11}$-Tz micro-SPECT/CT imaging (A/B ratio: 8.13 ± 2.51 vs 3.71 ± 1.55; $P < 0.001$; Figure 5B–D).

Findings of ex vivo Aortic BSGI, Pathological Examination, and Western Blot Analysis

In planar BSGI imaging of the aortas from AA mice excised immediately after anti-CD11b-TCO pre-targeted ^{99m}Tc-HYNIC-PEG$_{11}$-Tz SPECT/CT imaging, intensive radioactivity was observed in the AA area (Figure 5C). Interestingly, relative lower accumulation of radioactivity was observed in the AA area of IgG-TCO pre-targeted ^{99m}Tc-HYNIC-PEG$_{11}$-Tz-based BSGI images of AA mice (Figure 5B) and in the aortic arch area of anti-CD11b-TCO pre-targeted ^{99m}Tc-HYNIC-PEG$_{11}$-Tz-based BSGI images of mice from the control group (Figure 5A). The radioactivity distribution observed in planar imaging was consistent with the macroscopic features of the dissected aortas and the corresponding results of SPECT/CT. HE staining and anti-CD11b-based immunofluorescence findings showed that the AA lesions that

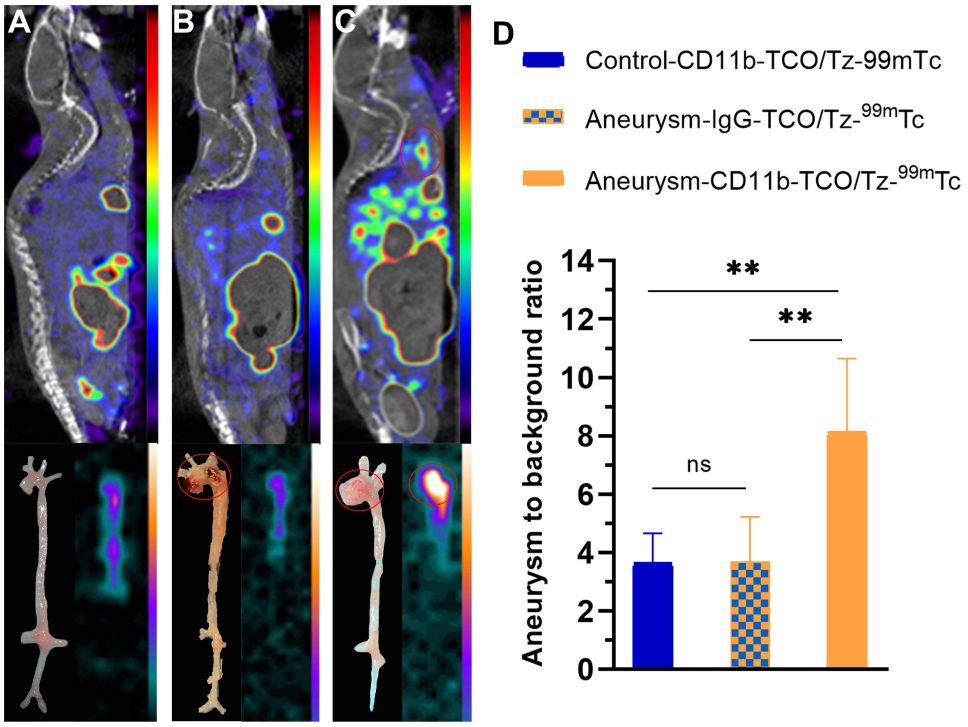

Figure 5 Validation of SPECT/CT imaging. Sagittal SPECT/CT images, dissected aortas, and ex vivo BSGI planar imaging of a control mouse (**A**) and AA mouse (**B** and **C**) obtained at 24 h after administration of anti-CD11b-TCO (**A** and **C**) and isotype IgG-TCO (**B**), and 2 h after injecting ^{99m}Tc-HYNIC-PEG$_{11}$-Tz. (**D**) Statistical comparisons of radioactivity uptake in AA lesions or the aortic arch between groups. **Indicates statistical significance at *P* values of <0.01.
Abbreviation: NS, the difference is not significant.

had obvious radioactivity accumulation in SPECT/CT images were anatomically confirmed aneurysms with infiltration of CD11b$^+$ inflammatory cells (Figure 6). Western blot assay demonstrated significantly higher expression of CD11b and MMP-9 in both the AA and AD sites ($P < 0.01$, Figure 7) than in the corresponding aortic areas of mice from control group.

Discussion

The present study describes a new pre-targeting SPECT/CT imaging method for the diagnosis of AA based on detection of the inflammatory marker CD11b, as inflammatory cells plays an important role in the early stages of AA. Early-stage diagnosis of AA based on the currently available methods is difficult, so this method may present a promising solution for the early diagnosis and treatment of AA.

There are several methods for the construction of animal models of AA. A commonly used method is feeding ApoE$^{-/-}$ mice with a high-fat die, but the incidence rate of AA is low and the risk to induce atherosclerosis is high in such model.[6,9,10] Another method is chemical stimulation through subcutaneous injection of angiotensin II or infusion of elastase or calcium chloride in the aorta. This technique is an efficient way to quickly induce AA at a relatively high incidence rate and with a high amplitude of inflammation. However, this method requires exposure of the aorta and is associated with high mortality rate, and thus is unsuitable for pre-targeting imaging which requires administration of the imaging agent twice within a short time interval. Furthermore, the pathophysiological process of AA induced by these methods is different from the development of AA in vivo conditions.[20] In contrast, ingestion of BAPN—an inhibitor of lysine oxidase that can induce degeneration of the aortic elastic layer—by adding it in the drinking water of mice mimics better the in vivo development of AA, and has been applied to establish abdominal AA and AD.[21] Therefore, this mouse model was used in the current study. The mice showed a stable and acceptable incidence rate (65.22%) and a low mortality rate (17.39%) when they were fed an appropriate concentration (0.4–0.5%) of BAPN. Furthermore, with this method, the induction of AA is more consistent

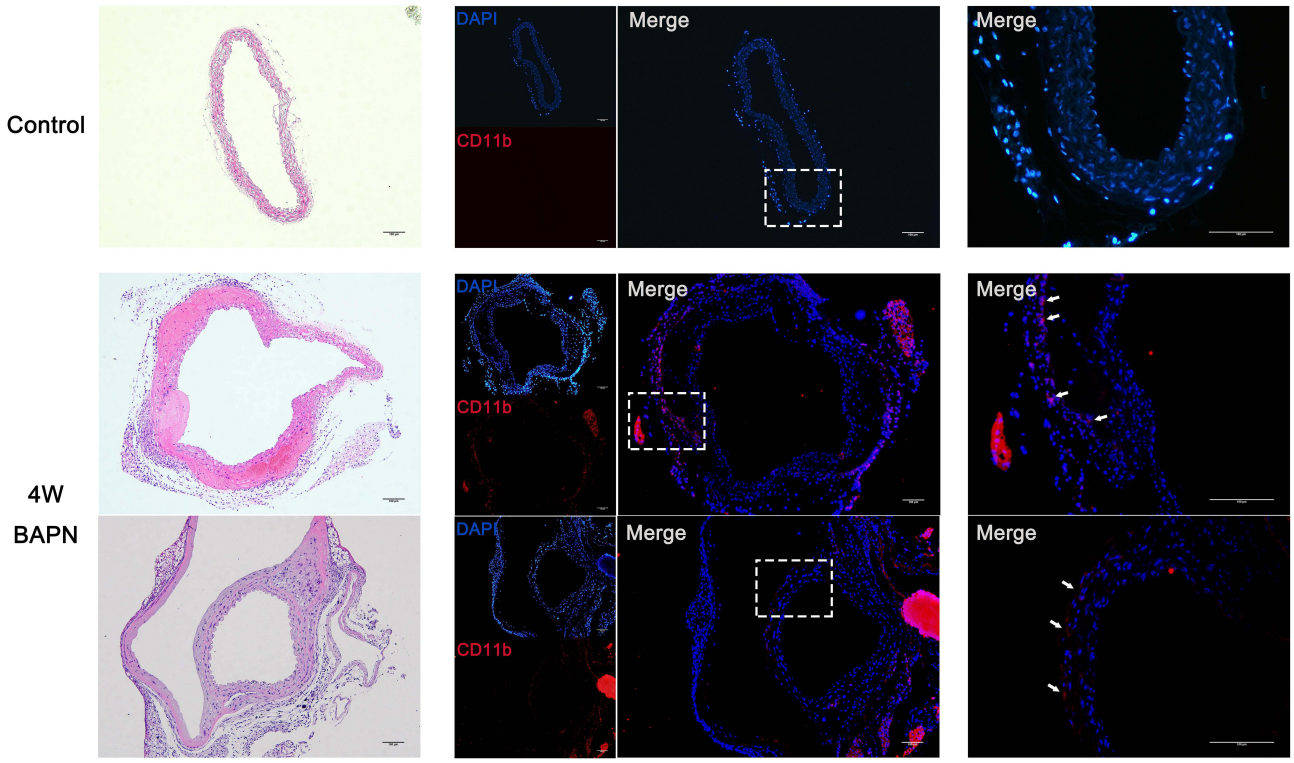

Figure 6 Immunohistochemical findings. H&E staining and CD11b immunofluorescence staining of AA. Control group: H&E staining showed no aortic dilation and the absence of immunofluorescence. Experimental group: H&E staining showed aorta dilation compared with the control group. Immunofluorescence staining showed infiltration of CD11b-positive cells (white arrows).

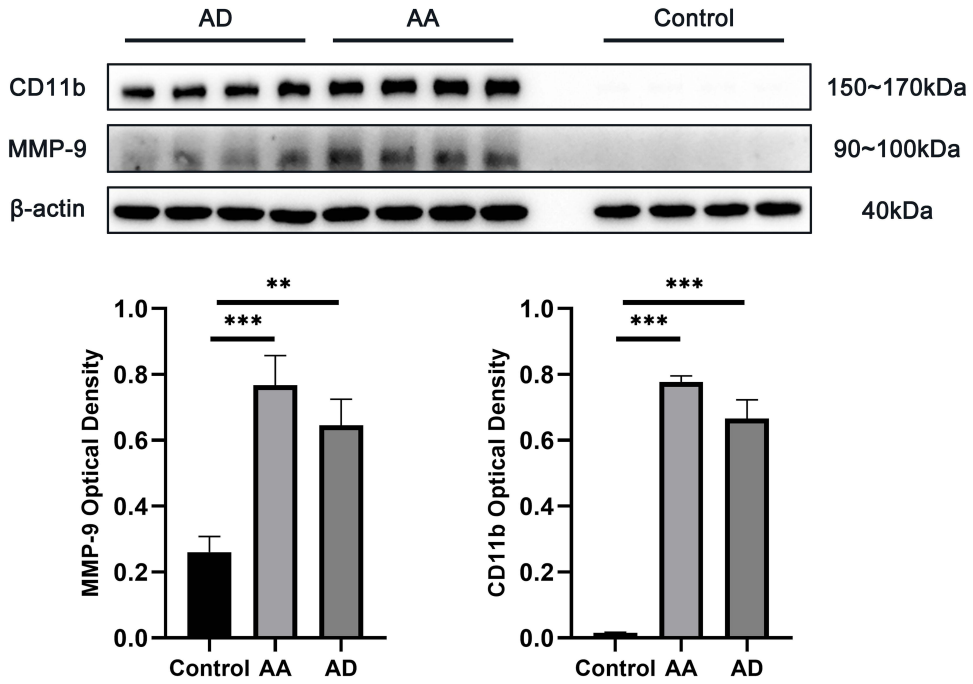

Figure 7 Western blot results for CD11b and MMP-9. The aortas of the control group mice were not positive for CD11b or MMP-9, while the AA and AD lesions demonstrated considerably high expression of CD11b and MMP-9 compared with control group. The expression level of β-actin (which was used as the internal control) was the similar in both groups. ** and *** indicate statistical significance at *P* values of <0.01 and <0.001, respectively.

with the pathophysiological process of AA formation linked to the infiltration of inflammatory cells.[22,23] As our method involved the imaging-based detection of inflammatory cells, this model was apt for our experiment.

In the current study, we modified anti-CD11b-Ab with TCO (anti-CD11b-Ab-TCO) for pre-targeting inflammatory cells[11,24] and fabricated ^{99m}Tc-HYNIC-PEG$_{11}$-Tz for SPECT/CT imaging. Firstly, the in vitro clicked anti-CD11b-Ab-TCO/^{99m}Tc-HYNIC-PEG$_{11}$-Tz showed high affinity and specificity for the CD11b-positive Raw-264.7 macrophage cells, which constitute the majority of inflammatory cells. This finding is consistent with those of previous studies.[12,25] Further, the pre-targeted imaging method successfully identified inflammatory AA lesions with high infiltration of CD11b-positive cells. The effective and specific affinity between the anti-CD11b antibody and inflammatory cells that infiltrated AA lesions was confirmed by ex vivo BSGI planar imaging, immunohistochemistry staining, and Western blot assay. Additionally, the small molecular weight of the fabricated ^{99m}Tc-HYNIC-PEG$_{11}$-Tz ensured its rapid clearance, and this reduced the possibility of radiation damage to un-targeted organs. Thus, our pre-targeted strategy is suitable for antibody-based imaging of inflammation-enrich AA.

Inflammatory cells are not the only biomarkers for molecular imaging of aortic disease. MMPs, vascular smooth muscle cell apoptosis, and collagen VI have also been found to be efficient targets for imaging aortic aneurysm or dissection.[26–28] MMPs (especially MMP-9) are mainly secreted by inflammatory cells, and are the main cause of extracellular matrix remodeling and vascular smooth muscle cell apoptosis.[29] In turn, MMP upregulation partially facilitates the recruitment of inflammatory cells and aggravates aortic lesion processes. Accordingly, in the current study, we found a consistent increase in the expression of the macrophage biomarker CD11b and MMP-9 (Figure 7). Of the inflammatory cells, macrophages play the main role in the early stage of AA; thus, macrophage infiltration may be an important biomarker for the diagnosis of AA in the early stage.[10,30]

Many imaging probes in nuclear medicine have been fabricated for targeting inflammatory cells or their apoptosis in vascular diseases in recent years, but most of these are limited to monocytes/macrophages.[26,31–34] However, it has been reported that other than monocytes/macrophages, 4.3% and 6.1% of the total cells that infiltrated AA were neutrophils and lymphocytes, respectively.[35] In addition, 11.8%, 0.7%, and 10.8% of the total infiltrating inflammatory cells were found to be neutrophils, lymphocytes, and other inflammatory cells, respectively, in atherosclerosis, which shares a similar inflammatory process with AA in the early stage.[36] Importantly, all these cells express CD11b.[35,36] This means that nuclear imaging probes that merely target monocytes/macrophages associated with AA may lead to a signal loss of about 10–23% compared to CD11b-targeting probes. Therefore, the imaging method proposed in this study might have certain advantages over previously reported imaging with nuclear probes, but further experiments are needed to confirm this speculation.

Conclusions

In this study, we demonstrated that SPECT/CT imaging using the anti-CD11b-TCO/Tz-PEG$_{11}$-HYNIC-^{99m}Tc-based pre-targeting strategy allows for detection of inflammation in progressive AA. With the use of this imaging strategy, inflammation-rich AA lesions can be identified in the early stage of the disease and the effectiveness of inflammation-targeted therapies in AA can be investigated.

Data Sharing Statement

The dataset used and/or analysed during the current study is available from the corresponding author on reasonable request.

Acknowledgments

We would like to thank for the technical supports from Prof. Shaoli Song and Dr. Jianping Zhang from Center of Biomedical Imaging, Fudan University, and Shanghai Engineering Research Center of Molecular Imaging Probes.

Funding

This study was funded by the National Natural Science Foundation of China (grant number: 81701730 and 81901796), the Shanghai "Rising Stars of Medical Talent"–Youth Development Program (grant number: HWJRS2019-72), the

Shanghai Sailing Program Supported by Shanghai Science and Technology Commission (grant number: 19YF1408300), and the Shanghai Municipal Key Clinical Specialty Project (grant number: SHSLCZDZK03401).

Disclosure

The authors declare that there is no conflicts of interest regarding this article.

References

1. Erbel R, Aboyans V, Boileau C, et al. ESC guidelines on the diagnosis and treatment of aortic diseases: document covering acute and chronic aortic diseases of the thoracic and abdominal aorta of the adult. The task force for the diagnosis and treatment of aortic diseases of the European Society of Cardiology (ESC). *Eur Heart J*. 2014;2014(35):2873–2926.
2. Kim JB, Spotnitz M, Lindsay ME, et al. Risk of aortic dissection in the moderately dilated ascending aorta. *J Am Coll Cardiol*. 2016;68:1209–1219. doi:10.1016/j.jacc.2016.06.025
3. Weinsaft JW, Devereux RB, Preiss LR, et al. Aortic dissection in patients with genetically mediated aneurysms: incidence and predictors in the genTAC registry. *J Am Coll Cardiol*. 2016;67:2744–2754. doi:10.1016/j.jacc.2016.03.570
4. Milewicz DM, Ramirez F. Therapies for thoracic aortic aneurysms and acute aortic dissections. *Arterioscler Thromb Vasc Biol*. 2019;39:126–136. doi:10.1161/ATVBAHA.118.310956
5. Sampson UK, Norman PE, Fowkes FG, et al. Global and regional burden of aortic dissection and aneurysms: mortality trends in 21 world regions, 1990 to 2010. *Glob Heart*. 2014;9:171–180. doi:10.1016/j.gheart.2013.12.010
6. GUO D, CL PAPKE, HE R, et al. Pathogenesis of thoracic and abdominal aortic aneurysms. *Ann NY Acad Sci*. 2006;1085:339–352. doi:10.1196/annals.1383.013
7. Andreata F, Syvannarath V, Clement M, et al. Macrophage CD31 signaling in dissecting aortic aneurysm. *J Am Coll Cardiol*. 2018;72:45–57. doi:10.1016/j.jacc.2018.04.047
8. Ruddy JM, Jones JA, Spinale FG, et al. Regional heterogeneity within the aorta: relevance to aneurysm disease. *J Thorac Cardiovasc Surg*. 2008;136:1123–1130. doi:10.1016/j.jtcvs.2008.06.027
9. Del PF, Di Gioia C, Tritapepe L, et al. The multitasking role of macrophages in Stanford type A acute aortic dissection. *Cardiology*. 2014;127:123–129. doi:10.1159/000355253
10. Khokha R, Murthy A, Weiss A. Metalloproteinases and their natural inhibitors in inflammation and immunity. *Nat Rev Immunol*. 2013;13:649–665. doi:10.1038/nri3499
11. Faridi MH, Maiguel D, Barth CJ, et al. Identification of novel agonists of the integrin CD11b/CD18. *Bioorg Med Chem Lett*. 2009;19:6902–6906. doi:10.1016/j.bmcl.2009.10.077
12. Liu G, Hu Y, Xiao J, et al. 99mTc-labelled anti-CD11b SPECT/CT imaging allows detection of plaque destabilization tightly linked to inflammation. *Sci Rep*. 2016;6:20900. doi:10.1038/srep20900
13. Boerman OC, van Schaijk FG, Oyen WJ, et al. Pretargeted radioimmunotherapy of cancer: progress step by step. *J Nucl Med*. 2003;44:400–411.
14. Rossin R, Lappchen T, van den Bosch SM, et al. Diels-Alder reaction for tumor pretargeting: in vivo chemistry can boost tumor radiation dose compared with directly labeled antibody. *J Nucl Med*. 2013;54:1989–1995. doi:10.2967/jnumed.113.123745
15. Rossin R, Verkerk PR, van den Bosch SM, et al. In vivo chemistry for pretargeted tumor imaging in live mice. *Angew Chem Int Ed Engl*. 2010;49:3375–3378. doi:10.1002/anie.200906294
16. Garcia MF, Zhang X, Shah M, et al. (99m)Tc-bioorthogonal click chemistry reagent for in vivo pretargeted imaging. *Bioorg Med Chem*. 2016;24:1209–1215. doi:10.1016/j.bmc.2016.01.046
17. Qiu L, Lin Q, Si Z, et al. A pretargeted imaging strategy for EGFR-positive colorectal carcinoma via modulation of Tz-radioligand pharmacokinetics. *Mol Imaging Biol*. 2021;23:38–51. doi:10.1007/s11307-020-01539-z
18. Qiu L, Tan H, Lin Q, et al. A pretargeted imaging strategy for immune checkpoint ligand PD-L1 expression in tumor based on bioorthogonal Diels-Alder click chemistry. *Mol Imaging Biol*. 2020;22:842–853. doi:10.1007/s11307-019-01441-3
19. Meszaros LK, Dose A, Biagini SCG, et al. Hydrazinonicotinic acid (HYNIC) – coordination chemistry and applications in radiopharmaceutical chemistry. *Inorg Chim Acta*. 2010;363:1059–1069. doi:10.1016/j.ica.2010.01.009
20. Wang Y, Krishna S, Golledge J. The calcium chloride-induced rodent model of abdominal aortic aneurysm. *Atherosclerosis*. 2013;226:29–39. doi:10.1016/j.atherosclerosis.2012.09.010
21. Ren W, Liu Y, Wang X, et al. beta-Aminopropionitrile monofumarate induces thoracic aortic dissection in C57BL/6 mice. *Sci Rep*. 2016;6:28149. doi:10.1038/srep28149
22. Nagashima H, Uto K, Sakomura Y, et al. An angiotensin-converting enzyme inhibitor, not an angiotensin II type-1 receptor blocker, prevents β-aminopropionitrile monofumarate-induced aortic dissection in rats. *J Vasc Surg*. 2002;36:818–823. doi:10.1016/S0741-5214(02)00139-8
23. Kanematsu Y, Kanematsu M, Kurihara C, et al. Pharmacologically induced thoracic and abdominal aortic aneurysms in mice. *Hypertension*. 2010;55:1267–1274. doi:10.1161/HYPERTENSIONAHA.109.140558
24. Yang XD, Ai W, Asfaha S, et al. Histamine deficiency promotes inflammation-associated carcinogenesis through reduced myeloid maturation and accumulation of CD11b+Ly6G+ immature myeloid cells. *Nat Med*. 2011;17:87–95. doi:10.1038/nm.2278
25. von Zur MC, von Elverfeldt D, Bassler N, et al. Superparamagnetic iron oxide binding and uptake as imaged by magnetic resonance is mediated by the integrin receptor Mac-1 (CD11b/CD18): implications on imaging of atherosclerotic plaques. *Atherosclerosis*. 2007;193:102–111. doi:10.1016/j.atherosclerosis.2006.08.048
26. Hu C, Tan H, Lin Q, et al. SPECT/CT imaging of apoptosis in aortic aneurysm with radiolabeled duramycin. *Apoptosis*. 2019;24:756–757. doi:10.1007/s10495-019-01563-7
27. Toczek J, Ye Y, Gona K, et al. Preclinical evaluation of RYM1, a matrix metalloproteinase-targeted tracer for imaging aneurysm. *J Nucl Med*. 2017;58:1318–1323. doi:10.2967/jnumed.116.188656

28. Xu K, Xu C, Zhang Y, et al. Identification of type IV collagen exposure as a molecular imaging target for early detection of thoracic aortic dissection. *Theranostics*. 2018;8:437–449. doi:10.7150/thno.22467
29. Kurihara T, Shimizu-Hirota R, Shimoda M, et al. Neutrophil-derived matrix metalloproteinase 9 triggers acute aortic dissection. *Circulation*. 2012;126:3070–3080. doi:10.1161/CIRCULATIONAHA.112.097097
30. Lindholt JS, Shi GP. Chronic inflammation, immune response, and infection in abdominal aortic aneurysms. *Eur J Vasc Endovasc Surg*. 2006;31:453–463.
31. Gaemperli O, Shalhoub J, Owen DR, et al. Imaging intraplaque inflammation in carotid atherosclerosis with 11C-PK11195 positron emission tomography/computed tomography. *Eur Heart J*. 2012;33:1902–1910. doi:10.1093/eurheartj/ehr367
32. Kaufmann BA, Carr CL, Belcik JT, et al. Molecular imaging of the initial inflammatory response in atherosclerosis: implications for early detection of disease. *Arterioscler Thromb Vasc Biol*. 2010;30:54–59. doi:10.1161/ATVBAHA.109.196386
33. Cheng D, Li X, Zhang C, et al. Detection of vulnerable atherosclerosis plaques with a dual-modal single-photon-emission computed tomography/magnetic resonance imaging probe targeting apoptotic macrophages. *ACS Appl Mater Interfaces*. 2015;7:2847–2855. doi:10.1021/am508118x
34. Hu Y, Liu G, Zhang H, et al. A comparison of [(99m)Tc] duramycin and [(99m)Tc] annexin V in SPECT/CT imaging atherosclerotic plaques. *Mol Imaging Biol*. 2018;20:249–259. doi:10.1007/s11307-017-1111-9
35. Nahrendorf M, Keliher E, Marinelli B, et al. Detection of macrophages in aortic aneurysms by nanoparticle positron emission tomography-computed tomography. *Arterioscler Thromb Vasc Biol*. 2011;31:750–757. doi:10.1161/ATVBAHA.110.221499
36. Majmudar MD, Yoo J, Keliher EJ, et al. Polymeric nanoparticle PET/MR imaging allows macrophage detection in atherosclerotic plaques. *Circ Res*. 2013;112:755–761. doi:10.1161/CIRCRESAHA.111.300576